

Star Formation in the starburst cluster in NGC 3603

Matteo Correnti • Francesco Paresce •
 Rossella Aversa • Giacomo Beccari •
 Guido De Marchi • Marcella Di Criscienzo •
 Xiaoying Pang • Loredana Spezzi • Elena Valenti •
 Paolo Ventura

Abstract We have used new, deep, visible and near infrared observations of the compact starburst cluster in the giant HII region NGC 3603 and its surroundings with the WFC3 on HST and HAWK-I on the VLT to study in detail the physical properties of its intermediate mass ($\sim 1 - 3 M_{\odot}$) stellar population. We show that after correction for differential extinction and actively accreting stars, and the study of field star contamination,

strong evidence remains for a continuous spread in the ages of pre-main sequence stars in the range ~ 2 to ~ 30 Myr within the temporal resolution available. Existing differences among presently available theoretical models account for the largest possible variation in shape of the measured age histograms within these limits. We also find that this isochronal age spread in the near infrared and visible Colour-Magnitude Diagrams cannot be reproduced by any other presently known source of astrophysical or instrumental scatter that could mimic the luminosity spread seen in our observations except, possibly, episodic accretion. The measured age spread and the stellar spatial distribution in the cluster are consistent with the hypothesis that star formation started at least 20-30 Myrs ago progressing slowly but continuously up to at least a few million years ago. All the stars in the considered mass range are distributed in a flattened oblate spheroidal pattern with the major axis oriented in an approximate South-East - North-West direction, and with the length of the equatorial axis decreasing with increasing age. This asymmetry is most likely due to the fact that star formation occurred along a filament of gas and dust in the natal molecular cloud oriented locally in this direction.

Matteo Correnti

INAF - Istituto di Astrofisica Spaziale e Fisica Cosmica, Via P. Gobetti, 101, I-40129 Bologna, Italy

Francesco Paresce

INAF - Istituto di Astrofisica Spaziale e Fisica Cosmica, Via P. Gobetti, 101, I-40129 Bologna, Italy

Rossella Aversa

INAF - Istituto di Astrofisica Spaziale e Fisica Cosmica, Via P. Gobetti, 101, I-40129 Bologna, Italy

Giacomo Beccari

ESO - European Southern Observatory, Karl-Schwarzschild-Str. 2, D-85748 Garching bei München, Germany

Guido De Marchi

ESA, Space Science Department, Keplerlaan 1, 2200 AG Noordwijk, The Netherlands

Marcella Di Criscienzo

INAF - Osservatorio Astronomico di Roma, Via Frascati 33, Monte Porzio Catone, Roma, Italy

Xiaoying Pang

Astronomisches Rechen-Institut, Heidelberg University, Heidelberg, Germany

Loredana Spezzi

ESA, Space Science Department, Keplerlaan 1, 2200 AG Noordwijk, The Netherlands

Elena Valenti

ESO - European Southern Observatory, Karl-Schwarzschild-Str. 2, D-85748 Garching bei München, Germany

Paolo Ventura

INAF - Osservatorio Astronomico di Roma, Via Frascati 33, Monte Porzio Catone, Roma, Italy

Keywords Stars: pre-main sequence - open cluster and associations: individual (NGC 3603)

1 Introduction

Hertzsprung-Russell (HR) or Colour-Magnitude Diagrams (CMDs) in combination with theoretical models can be used, in principle, to determine the age distribution of stars in a cluster. Measurable luminosity spreads in these diagrams have been found in many, if not all, young nearby and massive clusters measured to date. They can be interpreted as real age spreads

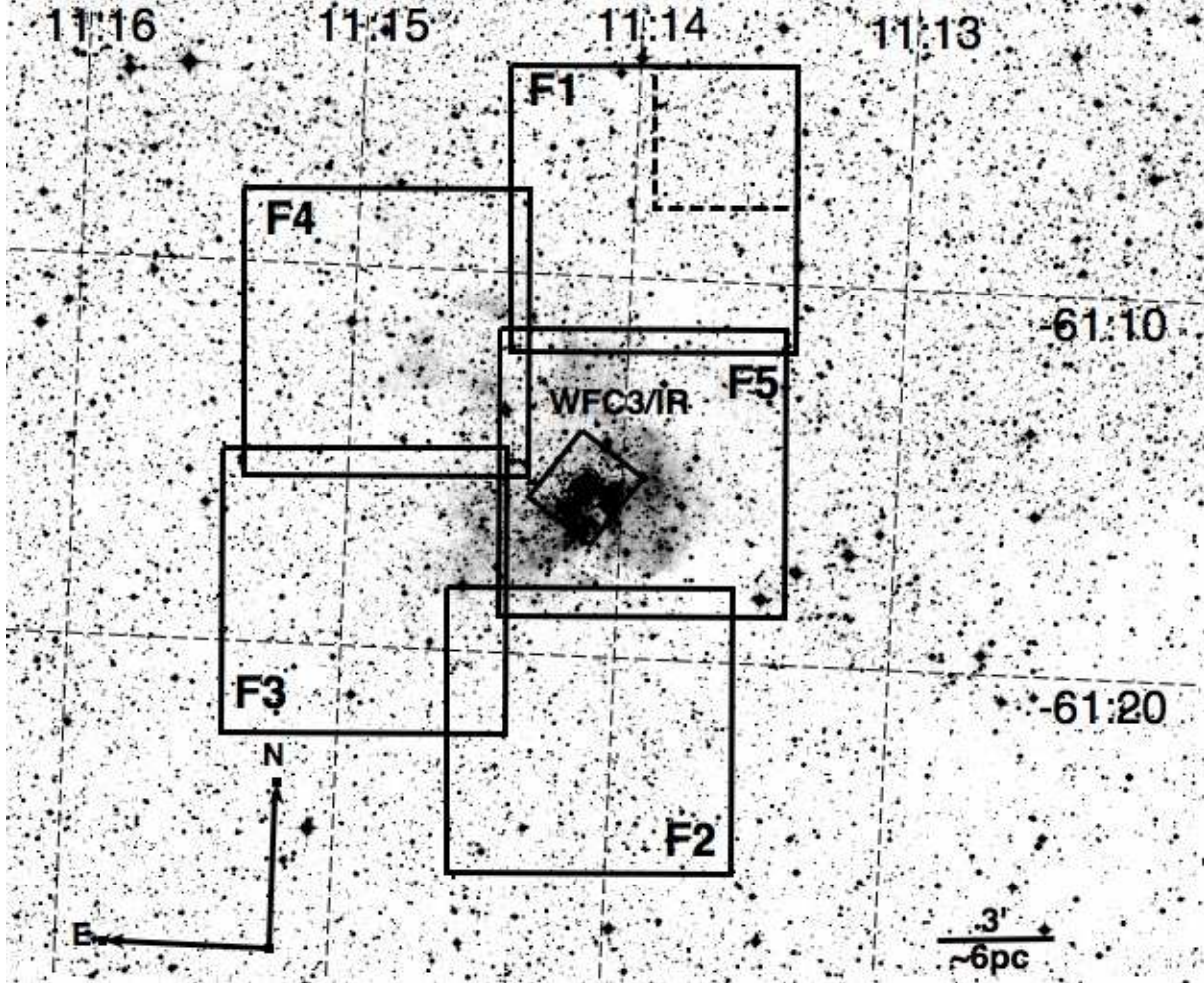


Fig. 1 WFC3 (small square) and HAWK-I (F1-F5) FoV plotted on the red Digitalized Sky Survey plates. Image centred at $RA(J2000) = 11^h15^m7^s.26$ and $Dec(J2000) = -61^\circ15'37''.9$, as determined by SB04. Orientation and size scale are also shown in the image. The position of frame 3 of field F1, used to derive the right hand CMD of Fig.3, is shown as a dashed square.

provided other sources of luminosity scatter can be defined accurately and their effects taken properly into account. These sources include, but may not be limited to, observational errors, differential extinction and reddening, distance uncertainties, field star contamination, unresolved multiplicity, variability and position shifts in the CMD due to the accretion process. The difficulties associated with identifying and quantifying this long list of possible non age dependent contributors to the luminosity spread has seriously hampered work in this field and created skepticism or ambiguity as to the reality of any claimed significant age spread in these clusters (Hartmann 2003; Hillenbrand 2009; Jeffries 2011).

In the specific case of the starburst cluster of radius $2.5'$ located in the giant HII region NGC 3603 (Nürnberg et al. 2002; Nürnberg & Petr-Gotzens 2002, hereafter NPG02) at a distance from the Sun of 6.0 ± 0.8 kpc (see Harayama, Eisenhauer & Martins 2008, for a complete discussion), the question of its age and possible spread has been hotly debated for some time. This cluster is one of the most compact and luminous massive star clusters in the Milky Way (MW), with a bolometric luminosity of 100 times that of the Orion Cluster, and a possible nearby prototype of the extragalactic starburst clusters like NGC 2070 in the Large Magellanic Cloud (LMC). Melnick, Tapia & Terlevich (1989) were the first to suggest on the basis of theoretical isochrones on a reasonably deep $V, B - V$ CMD, the existence of a small (± 2 Myr) real age spread around an average age of 2.5 Myr in mainly relatively massive Main Sequence (MS) stars with star formation seemingly propagating roughly from North to South. Some time later, on the other hand, Eisenhauer et al. (1998) using near infrared (IR) J, H, K ground based observations argued that their data were consistent with a single burst of star formation and that the cluster was actually a coeval group of stars of age 1-2 Myr with no need for any significant age spread. This conclusion essentially was echoed, with some variations, by subsequent investigators (Stolte et al. 2004; Sung & Bessell 2004, hereafter SB04).

More recently, Melena et al. (2008), although supporting these later conclusions for the most massive stars ($> 100M_{\odot}$) in the core, argue that lower mass objects ($20 - 40M_{\odot}$) may have a larger spread of 1-4 Myr. Harayama, Eisenhauer & Martins (2008, hereafter HEM08), also find for the lower mass Pre-Main Sequence (PMS) stars an average age of 0.7 Myr with a possible spread of only ± 0.3 Myr, but that for the heavier MS stars an upper age limit of 2.5 Myr is appropriate. Rochau et al. (2010) instead show that most

intermediate mass PMS stars in the core of the cluster have an age of 1 Myr but with a sparse population of low mass stars of age about 4 Myr.

Finally, Beccari et al. (2010, hereafter B10), working in the visible, using a much larger sample of stars and exploiting the technique of separating PMS cluster members from field objects on or near the Zero Age Main Sequence (ZAMS) using the $H\alpha$ line in emission (De Marchi, Panagia & Romaniello 2010) conclude that the single age or starburst hypothesis is not consistent with their data. Instead they indicate that the PMS cluster members distribute themselves essentially continuously across a wide range of ages between 1 and 30-40 Myr with a peak at a few Myr. This conclusion could, in principle, be negatively affected by the possible errors in isochronal ages discussed above. In any case, this large uncertainty in the correct age attribution of the cluster stars is a very important issue to resolve as it affects the crucial question of how and where star formation occurs in the progenitor Giant Molecular Cloud (GMC) of which the compact starburst cluster is only a small part. In particular, one can ask whether star formation in these clusters occurs in a slow ($\sim 10 - 20$ Myr) or fast (~ 1 Myr) mode and if it is localized or distributed over a large volume of the cloud. In this context, an important question left unanswered is whether or not the older $H\alpha$ emitting stars detected by B10 actually belong to the starburst cluster or whether they are part of a more spatially distributed population belonging to the much larger GMC surrounding it, much like the situation, for example, of the cluster Tr 14 and Tr 15 in the Carina nebula (Preibisch et al. 2011).

In order to tackle these issues, we have analyzed deep near IR Wide Field Camera 3 (WFC3) and High Acuity Wide field K-band Imager (HAWK-I) images of the starburst cluster in NGC 3603 (from now on simply referred to as NGC 3603). The WFC3 IR and HAWK-I datasets represent a significant improvement in accuracy in a wavelength region where high instrument sensitivity and lower interstellar gas extinction should lead to a much better determination and understanding of the variables involved in establishing the sources of the luminosity spread observed in the visible. In particular, the IR is best suited to minimize the effects of colour and luminosity shifts due to the accretion process in these PMS stars. In the visible CMD, the Ultraviolet (UV) excess emission in the V band from this process results in younger stars looking older and, thus, possibly biasing the putative age spread. In the IR CMD, on the other hand, the IR excess works in the opposite direction making older stars look younger with the result that the oldest population cannot be

contaminated by even older objects that don't exist. In addition, these two datasets allow us to sample the entire cluster together with its surroundings well into the vast majority of its stellar population. In this paper, we will consider and attempt to quantify the possible measurable sources of scatter in the HR diagram of the cluster, investigating evidence for and against age spread, and we will try to demonstrate that the scatter is most likely due to a real age effect and not to the "nuisance" sources listed above.

The plan of the paper is the following. In Sect. 2 we present the observations of NGC 3603 obtained with WFC3 and HAWK-I, while in Sect. 3 we describe the data reduction processes used to derive the sources' final catalogue. In Sect. 4 we present the analysis done on the CMDs with the histograms representing the number of PMS stars in the cluster in each age interval, as a function of age and our derivation of the structure and the spatial distribution of the cluster. In Sect. 5, we analyze the sources of uncertainty that can bias our work and we discuss how the results can be affected. Finally, we summarize and discuss our results in Sect. 6.

2 Observations

The photometric data used in this work consist of a series of deep multi-band images acquired with the WFC3 on board the Hubble Space Telescope (HST) and HAWK-I on the Very Large Telescope (VLT). Observations obtained with these two instruments are described in the next subsections.

2.1 WFC3 observations

The WFC3 consists of two detectors, one optimized for observations in the wavelength range 200 to 1000 nm (UVIS channel) and the other between 0.9 and 1.7 μm (IR channel). The UVIS detector consists of $2 \times 2K \times 4K$ thinned, backside illuminated, UV optimized e2v CCDs covering a field of view (FoV) of $162'' \times 162''$ at a plate scale of $0.04''/\text{px}$. The IR detector is a $1K \times 1K$ Teledyne HgCdTe FPA, MBE grown, substrate removed detector offering a total FoV of $123'' \times 136''$ at a pixel resolution of $0.13''$. A more detailed description of the WFC3 and its current performance can be found in Mackenty et al. (2010) and Wong et al. (2010).

The WFC3 data used in this work are part of the Early Release Science (ERS) observations obtained by the WFC3 Scientific Oversight Committee for the study of star forming regions in nearby galaxies (Program ID number 11360). NGC 3603 was observed using both

the UVIS and IR channels. The UVIS and IR datasets were presented in B10 and in Spezzi et al. (2011, hereafter S11), respectively. Briefly, in the IR, NGC 3603 was observed through the F110W (*J* band) and F160W (*H* band) broadband filters, the F127M, F139M and F153M medium-band filters, and the F128N narrow band filter. Three images were acquired for each band in order to allow for the removal of cosmic rays, hot pixels, and other detector blemishes. Details on the total exposures for each band are reported in Table 2 of S11. The position of the WFC3 field is shown in Fig. 1. The WFC3 *J* band image of the cluster has been presented in Fig. 1 of S11 and a five colour composite image can be found in the Hubble Heritage site: <http://heritage.stsci.edu/2010/22/index.html>.

2.2 HAWK-I observations

In addition to the WFC3 data, we used a series of observations obtained with HAWK-I, in order to sample the cluster stellar population beyond the central region in the IR. HAWK-I (see Kissler-Patig et al. 2008) is a near-IR imager at the ESO 8m (VLT-UT4, Yepun) equipped with a mosaic of four Hawaii 2RG 2048×2048 pixel detectors with a scale of $0.106''$ per pixel. The camera has a total FoV on the sky of $7.5' \times 7.5'$ with a small cross-shaped gap of $\sim 15''$ between the four detectors. The observations of NGC 3603 were performed in March 2009, in visitor mode, and retrieved from the ESO archive (Proposal ID: 082.C-0889(A), PI Nürnberg). The observing conditions were generally good, with an average seeing measured on image of $\sim 0.6''$. The data are derived from images taken through the standard broadband *J*, *H*, and *K_s* filters. A total of five fields were observed, one roughly centred on the cluster and four fields sampling the external regions around the cluster core (see Fig. 1) covering a total area of about 337 arcmin^2 . Each frame acquired through the *H* and *K_s* filters is the combination of 6 exposures each 10 sec long, while frames taken with the *J* filter are the result of 2 and 1 exposures each 30 and 60 sec long, respectively. For each filter and pointing the observation was repeated with a random dithering pattern and jitter box width of $30''$ until reaching a total exposure time of 10 min for each filter. As can be seen in Fig. 1, each field has a region of overlap with the adjacent ones, so that it is possible to check the accuracy of the astrometric and photometric calibrations.

3 Data reduction

The photometry of the entire WFC3 dataset was performed on the flat-fielded (FLT) images following a

standard Point Spread Function (PSF) fitting procedure with DAOPHOT II/ALLSTAR (Stetson 1987) package. An accurate PSF model for each image was obtained adopting a first-order polynomial on about 150 isolated and well exposed stars homogeneously distributed in the FoV. A master list of stars was obtained using stars detected in the F110W image (the deepest of the IR dataset) and was then used as input for ALLFRAME (Stetson 1994) to perform an accurate PSF fitting on all the images. All the magnitude values for each star were normalized to a reference frame and averaged together, and the photometric errors were derived as the standard deviation of the repeated measurements. The magnitudes were finally transformed into the VEGAMAG photometric system by adopting the recipe described in Kalirai et al. (2009, see S11 for details). The number of objects detected at least in one of the five filters is 9693.

The final WFC3 catalogue, obtained imposing that stars have been measured in each filters (i.e.: F110W, F160W, F127M, F128N, F139M and F153M), contains 8831 stars. Saturation of the WFC3 images occurs at $J \sim 12$ and $H \sim 11.5$, while stars are detected at 3σ accuracy down to $J = 20.5$ and $H = 19.5$, respectively. At the distance and typical age of NGC 3603, these limiting magnitudes correspond roughly to cluster members with masses in the range between 0.5 and $3.5 M_{\odot}$, according to the models of Di Criscienzo et al. (2009, hereafter DC09).

Photometry in the core region, out to a distance of $\sim 10''$ from the cluster centre derived by SB04 and adopted also in B10 is severely affected by strong camera saturation due to the high concentration of very bright young massive O-B stars. We decided to excise this region from our analysis, so the final catalogue does not include stars inside it, due to the fact that the completeness in this part is very low (see Sect. 3.1 for the discussion about completeness in the WFC3 and HAWK-I fields) and the photometric uncertainty is very high in the detected stars. After this cut, the final WFC3 catalogue contains 8553 stars.

For what concerns the HAWK-I data, we used standard IRAF routines to process them. For all filters, we derived a sky image from a median combination of the dithered images that we subtracted from each frame. To normalize the pixel-to-pixel response, all frames were divided by a normalized twilight flat. Finally, all the flat- and sky-corrected frames have been averaged in a single image for each of the three filters. In what follows, we refer to a frame as a combination of these sets. Aperture photometry was performed independently on each frame using the aperture photometry code SExtractor (Bertin & Arnouts 1996) and adopting

a fixed aperture radius of 4 pixels ($0.4''$). The lists of magnitudes for each filter were then combined with the requirement that each star had to be measured at the same time in the J , H and K_s bands. The mosaic of the five pointings samples a total of 110347 stars from the magnitude $J \sim 12$ down to $J \sim 22$ in an area of $\sim 15' \times 22.5'$ around the cluster centre. We estimate that objects as faint as $J \sim 21$, $H \sim 20$ and $K_s \sim 20$ are detected at a $S/N \geq 10$.

More than 10000 stars from the Two Micron All Sky Survey (2MASS, Skrutskie et al. 2006) catalogue, from a total sample of ~ 31000 2MASS sources in the area of the HAWK-I fields, were used as photometric and astrometric standards to obtain accurate photometric calibration of the J , H and K_s bands, and to transform the instrumental relative position of stars into J2000 celestial coordinates. The HAWK-I catalogue sampling the cluster central regions was adopted as catalogue of secondary astrometric standards in order to properly find an astrometric solution for the WFC3 catalogue. We estimate that the global uncertainty in the astrometric solution relative to 2MASS is $\sim 0.2''$. Magnitudes J , H and K_s of all the frames have been calibrated using the stars in common with 2MASS, typically ~ 200 stars for each of them, and the results of the calibration have been checked comparing the magnitude values for the stars in common between different fields, i.e.: the stars in the overlapping region. Each overlapping strip contains ~ 500 stars, except in the case of field F2 and F5, where the stars in common are ~ 300 . The differences in the independent calibration for the magnitudes J , H and K_s are of order $\sigma_j \sim 0.04$, $\sigma_H \sim 0.04$ and $\sigma_K \sim 0.05$, respectively reassuring us about the precision of the calibration through 2MASS.

To compare magnitudes derived from the WFC3 and from HAWK-I, and to build a single catalogue containing all the sources in the FoV, it is necessary that one of the magnitudes system is translated into the other, due to the different filters between WFC3 and HAWK-I. The J and H (F110W and F160W) magnitudes in the WFC3 system have been transformed to the HAWK-I (2MASS) system, using empirical transformations, derived from 3308 stars in common between the two fields. In particular, we obtained the *new* J and H adopting the following equations:

$$J = F110W - 0.111 - 0.246 * (F110W - F160W) \quad (1)$$

$$H = F160W - 0.049 - 0.175 * (F110W - F160W) \quad (2)$$

The final total catalogue, obtained combining WFC3 and HAWK-I fields, with the obvious prescription of not double counting the stars in the overlap regions, contains 112265 stars. For those stars having both a

WFC3 and HAWK-I measurement, only the more precise 2MASS calibrated WFC3 magnitude is retained in the final catalogue.

3.1 Completeness of WFC3 and HAWK-I fields

As the last step of the reduction process, we calculated the completeness in the WFC3 field and in four HAWK-I fields, from F1 to F4, selecting a different frame in each field, in order to avoid a possible bias. We do not calculate the completeness in each frame because the crowding conditions in the observed external fields are not critical and are very homogeneous in general. This suggests that the completeness level should be not very different from frame to frame. On the contrary, since the WFC3 field is very crowded and, as we have mentioned above, the central region is affected by strong camera saturation, due to the high concentration of very bright young massive O-B stars, the situation is more complex.

We performed extensive artificial star experiments in one frame for each field assumed to be representative of the whole field sample following the recipe described in Bellazzini et al. (2002). A total of nearly 150000 artificial test stars were added to each selected field. The artificial stars were uniformly distributed in each run into grids of cells so that the minimum distance between two artificial stars is of the order of ~ 5 Full Width Half Maximum (FWHM), in order to leave the crowding conditions unaltered. The test stars were distributed in magnitude according to a luminosity function similar to the observed one but monotonically increasing also beyond the limit of the photometry and with a colour distribution covering the full colour ranges of the observed stars. The entire reduction procedure has been repeated in the same way on each synthetically enriched image. We derive that the completeness factors for the four HAWK-I frames are the same within the errors in the range of magnitude analyzed ($12 \lesssim J \lesssim 18$). This is not unexpected since the crowding conditions are nearly similar, and in any case very far from the critical conditions found in the central region of the cluster. Furthermore, the spatial distribution of stars is very homogeneous so there is no expected variation of completeness with position. This result provides robust support for taking the derived completeness as representative of the whole HAWK-I fields, except the F5, since it has been demonstrated that the observed field-to-field variations have minimal impact on the overall completeness. Concerning the WFC3, the completeness factor, C_f , is $\geq 85\%$ for $J < 18$, in the external regions, while falls to lower values in the central ones due to crowding and saturation (see top panels of Fig. 2).

As stated before, in the HAWK-I fields instead, the behaviour of C_f is more linear and we derive a $C_f > 70\%$ for $J < 18$ in all the four analyzed frames (see bottom panels of Fig. 2). The completeness situation for field F5 is slightly different due its dependence on distance from the centre. In the external regions of this field, the completeness is similar to what we found for the other HAWK-I fields, i.e. $C_f > 70\%$ for $J < 18$, while it decreases in the crowded central portion of the field, in the region of overlap with the WFC3 field. However, it is worth noting that in this specific region, as mentioned at the end of the previous section (Sec. 3), we retain in the final catalogue only stars from the WFC3 catalogue, so the reference completeness is that of the WFC3 shown in the top panels of Fig. 2. These panels show that there is no variation with position and/or radial distance from the centre, so the combination of these two effects makes it unnecessary to consider the completeness variation encountered in the field F5, and to consider it in the same way as the other HAWK-I fields.

3.2 CMDs of WFC3 and HAWK-I fields

The result of the reduction process described above is shown in the form of two observed $J, J - H$ CMDs in Fig. 3. In the left panel, we have the CMD of the WFC3 field, representative of the central region of the cluster, while in the right panel we have the CMD of a frame of the F1 HAWK-I field (F1_3, see for a visual reference Fig. 1), well outside the nominal $2.5'$ radius of the cluster (NPG02). The HAWK-I field is chosen such that the areas are the same for a meaningful comparison.

Photometric colour and magnitude uncertainties are reported in both CMDs. The errors for the WFC3 CMD were derived as the simple standard deviations of the repeated measurements of the WFC3 field magnitudes, while photometric errors for the HAWK-I field have been derived from the mean values of the $mag_{in} - mag_{out}$ distribution, derived from the incompleteness simulations. In the WFC3 CMD, two distinct and well separated features are clearly visible: on the blue side, the almost vertical sequence around $J - H \sim 0.6 - 0.7$ bending to the red at $J \sim 18$, is consistent with a suitably reddened ZAMS of field and cluster stars (see also Sec. 4.4 and 4.5). On the red side, the wide clump of stars around $J - H \sim 1.3 - 1.4$ less evident at brighter magnitudes, but well populated from $J \sim 17.0$ to $J \sim 19.5$ is consistent with the position of cluster PMS stars. In support of this conjecture, in the right panel, the HAWK-I CMD clearly shows only the corresponding ZAMS of the field stars with no sign of the PMS clump. Hence, the different number of stars

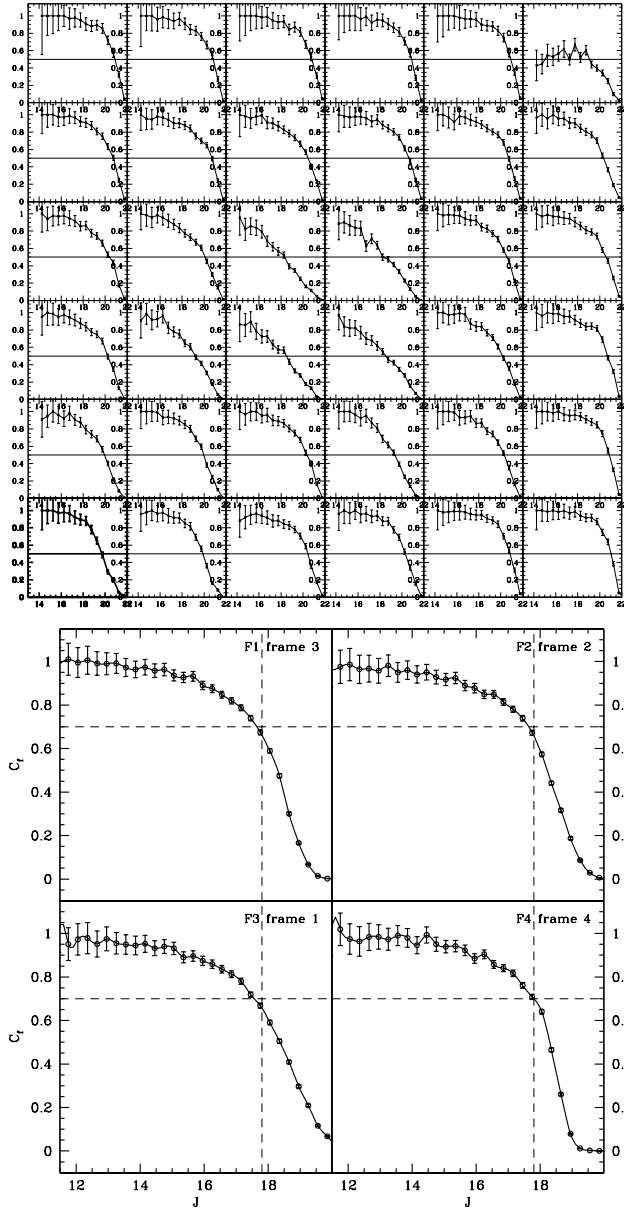


Fig. 2 Top panel: completeness factor as a function of J magnitude for different sub-regions in the WFC3 fov. The reported lines are best-fitting curves to the data. Completeness does not show variations with position and/or radial distance from the centre; the four central panel show the low C_f in the excised central region (i.e.: region inside a radius of $10''$ from cluster centre). Bottom panel: completeness factor as a function of J magnitude for the four analyzed frames of the four different HAWK-I fields. Also in this case, the reported lines are best-fitting curves to the data. The completeness factor is similar in all the four analyzed frames. Our limiting magnitude ($J = 17.83$) and a $C_f = 0.7$ (i.e. : 70%) are also indicated (dashed vertical and horizontal lines, respectively).

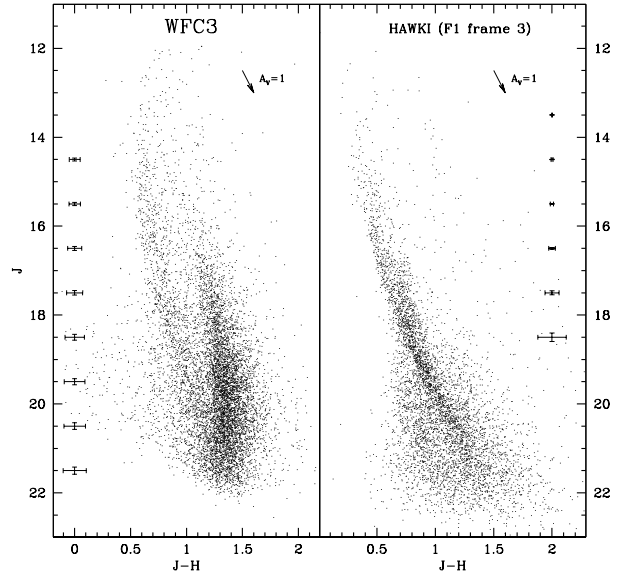


Fig. 3 Observed $J, J-H$ CMDs of the WFC3 field (left panel), representative of the central region of the cluster, and of the frame 3 of HAWK-I field F1 (right panel), which position is reported in Fig.1, sampling the external regions. Both CMDs have been obtained using fields of the same area. Photometric colour and magnitude uncertainties are reported in both CMDs. For the HAWK-I one, we obtained them from completeness simulations. (comparison between the input magnitudes and the output ones). The reddening vector ($A_V=1$) is also shown.

and the different shape of the two CMDs are not due to crowding, photometric uncertainties or completeness but to the different population of stars we are observing.

4 Analysis

4.1 Reddening Correction

The data discussed above were dereddened using different approaches for the two datasets. B10 and S11 obtained dereddened magnitudes of the stars in the WFC3 FoV by exploiting the extinction study of NGC 3603 by SB04. These authors found that the value $A_V = 4.5$ is representative of the very centre of the cluster while there is an increase toward the external regions. Adopting the total-to-selective extinction ratio (R_V) value of 3.55, suggested by SB04, B10 estimated that the value $A_V = 5.5$ is representative of the mean visual extinction in the area sampled by the WFC3 observations. S11 adopted this value of A_V and the extinction law of Cardelli, Clayton & Mathis (1989) to derive the following extinction for J and H magnitudes: $A_J \sim 2.00$ and $A_H \sim 1.05$, respectively. Following S11, we adopted these values to correct the magnitudes of stars in our catalogue for the WFC3 field.

Concerning the HAWK-I fields, instead, we adopted the approach suggested by HEM08, namely that in the observed CMDs for each field, we determine the position of the mean ridge line of the ZAMS that is the predominant feature present in the external CMDs as seen for example in the right panel of Fig. 3. As a theoretical template, we adopt the ZAMS by DC09. The idea is that, if there is a discrepancy in the two ZAMS (observed vs theoretical), the only free parameter that allows us to shift the mean ridge line in the colour-magnitude plane representing the observed ZAMS is the extinction A_V . Therefore we used a χ^2 test to derive the A_V value for which the difference in colour and magnitude between the mean ridge line representing the observed ZAMS and the theoretical ZAMS is minimum. This process has been applied to each frame of HAWK-I fields so that we can obtain a frame-to-frame reddening correction. We observed that fields on the northern side (F1 and some frames of F4) have a lower extinction respect to the central field and, above all, respect to the southern ones.

In detail, we have that the mean value of extinction, $\langle A_V \rangle$, for each field is the following: $A_V = 4.3 \pm 0.2$ for F1, $A_V = 5.1 \pm 0.3$ for F2, $A_V = 4.9 \pm 0.4$ for F3, $A_V = 5.0 \pm 0.4$ for F4 and finally $A_V = 4.9 \pm 0.4$ for F5. Thus it is clear that the choice of a single value of A_V

for all the HAWK-I fields would lead to an overestimate of the extinction in the majority of frames and more in general in the observed fields.

In conclusion, the magnitudes of stars in the final catalogue have been corrected in the appropriate manner, depending on their position. All the results in the following, if not explicitly said, have been obtained using this reddening correction obtained with the prescription described above.

4.2 Theoretical models and age histograms

The dereddened data were used to determine the age distribution of PMS stars in the cluster. In Fig. 4, we show the dereddened $J_0, (J - H)_0$ ¹ CMD of the entire cluster, namely a region with a radius of $2.5'$ from the cluster centre, derived exploiting the WFC3+HAWK-I catalogue. We use here the radius for the cluster given by NPG02. The position of the ZAMS is taken from DC09 for solar metallicity (dashed line), having adopted a distance modulus $(m - M)_0 = 13.90$ (see HEM08 and references therein). Together with the ZAMS we also plot the PMS theoretical isochrones of DC09, for ages 2, 5, 10, 20, 30 Myr. This set of isochrones is characterized by a non grey atmosphere and $\alpha = 1.5$, where α is the parameter representing the convection efficiency (see Sect. 5.3 and the Appendix A for a detailed description of the prescriptions and processes necessary to obtain them). Stars located above the 2 Myr isochrone, i.e. $J \sim 13$ and $J - H \sim 0.55$, are mainly stars younger than 1-2 Myr. In addition, a small fraction of these are probably stars having a different reddening respect to the mean value adopted in this work so that they have been corrected with a wrong value of reddening and they would need in principle to be shifted in the CMD. Note that the photometric uncertainty of our data (see crosses in Fig. 4) confirms that it is possible to assign relative ages to these stars with an accuracy of a factor of 2.

In principle, age histograms are an excellent tool to determine the age distribution of stars in clusters. To obtain them, we need to count objects in each age interval limited by the position of the isochrones in CMDs. The process is not trivial in the IR because, as can be seen in Fig. 4, isochrones are not always parallel to each other, in contrast with what happens in the visible (see for example Fig. 3 of B10). In the IR, they start to cross at $J \sim 17.8$, so we must exclude stars fainter than this limit, considering only brighter sources in our analysis. In fact, without this magnitude cut, older PMS

¹For brevity, in the following, if not explicitly stated, all the reported magnitudes and colours are reddening-corrected (i.e., for example, $J = J_0 =$ extinction corrected J magnitude)

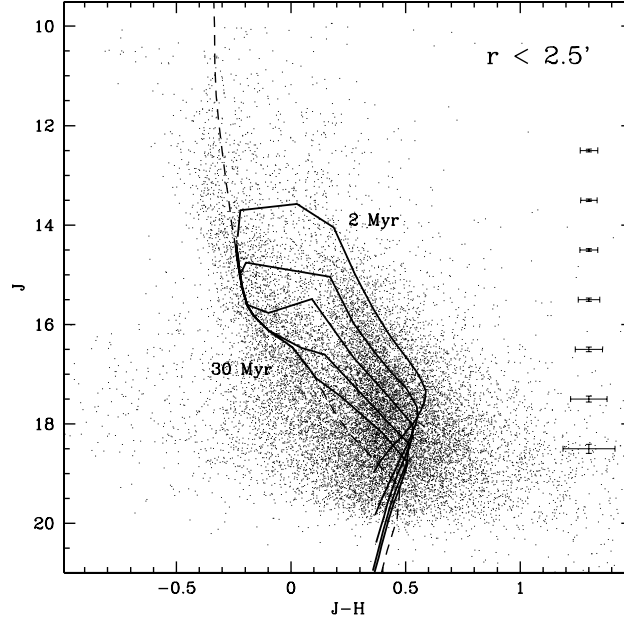


Fig. 4 Dereddened $J, J - H$ CMD using stars located inside the nominal radius $r = 2.5'$ (from NPG02) of the cluster. The dashed line is the ZAMS from DC09, for solar metallicity and adopting a distance modulus $(m - M)_0 = 13.90$. The population of PMS stars is fitted with 2, 5, 10, 20, 30 Myr PMS isochrones (from DC09) (solid lines). The position of the 2 and 30 Myr isochrones is indicated. On the right side the photometric colour and magnitude uncertainty are reported.

stars, on the blue side of the CMD, would be artificially more numerous than younger ones. On the other hand, the brightest magnitude we can consider is reached at $J \sim 13.6$ by the 2 Myr isochrone.

Thus, the actual magnitude range, in which we can perform our counts, is $13.6 < J < 17.8$ corresponding roughly to a mass range from 1 to $3 M_{\odot}$. This sample corresponds to $\simeq 30\%$ (~ 5000) of the total number of the stars detected in the cluster. We used as a lower age limit the isochrone of 2 Myr because younger isochrones cross the older ones at brighter magnitudes (the 1 Myr isochrone crosses the 2 Myr one at $J \sim 17$), thus reducing the range of analysis. Moreover, we selected this lower limit also because at lower magnitudes (i.e. $J \sim 18 - 19$) the completeness factor C_f is much lower and the photometric uncertainties on the $J - H$ colour are comparable, if not bigger, than the typical isochrone separation; so our conservative choice eliminates the possibility of systematic errors in the age determination of stars. We also decided to use the ZAMS as the blue colour limit since, as we will see clearly in the density profile and maps shown in Sect. 4.5, a good fraction of old ($\sim 20 - 30$ Myr) cluster PMS stars are actually located near the ZAMS and would be excluded from our sample using a redder limit. The corresponding age distribution of the stars in Fig. 4 is shown in the form of a logarithmic histogram in Fig. 5. This figure clearly shows that star formation in NGC 3603

has been ongoing for at least 20-30 Myr and no visible gaps are present, or at least evident, with the level of age resolution we adopted (a logarithmic bin of 0.3, corresponding to a factor of 2 in age).

4.3 Comparison between UVIS and IR histograms

To test the results obtained with the DC09 theoretical models in the IR, we compared them with the histogram obtained in the UV with the same models. In the top panels of Fig. 6, we show the $V, V - I$ and $J, J - H$ CMDs in the WFC3 FoV, with, superimposed, 2, 5, 10, 20, 30 Myr isochrones, from DC09. As already said, we observe that in the UV CMD the isochrones are parallel to each other and so it is possible to extend the analysis to redder colours (i.e.: younger stars), while in the IR CMD we are limited by the shape of the isochrones that at a given magnitude (depending on the model) start to cross each other. To have a direct comparison between the resulting histograms, therefore, we excluded the age range from 1 to 2 Myr given by the UV theoretical models and we limited the analysis to the magnitude range $16 < V < 20$. The bottom panels of Fig. 6 show the logarithmic histograms representing the age distribution of stars in the two cases. In both histograms, the age spread is present and the two distributions are quite similar in shape within the adopted age uncertainty of a factor of two.

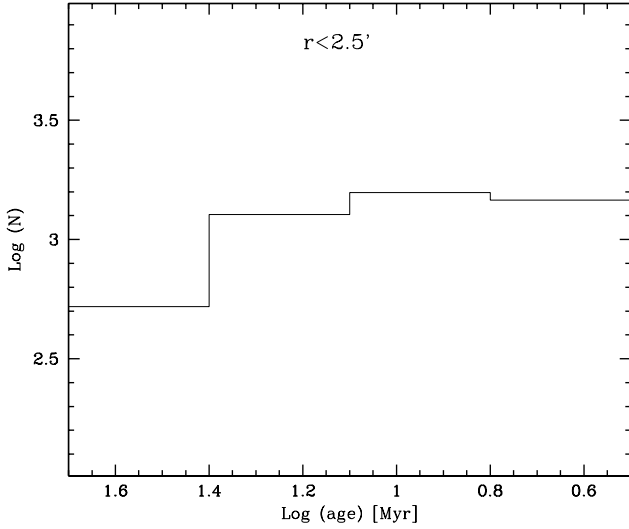


Fig. 5 Logarithmic histogram representing the number of PMS stars in the cluster with magnitude range $13.6 < J < 17.8$, in each age interval, as a function of age. The histogram is derived using stars located inside the nominal radius $r = 2.5'$ (NPG02) and isochrones as in Fig. 4

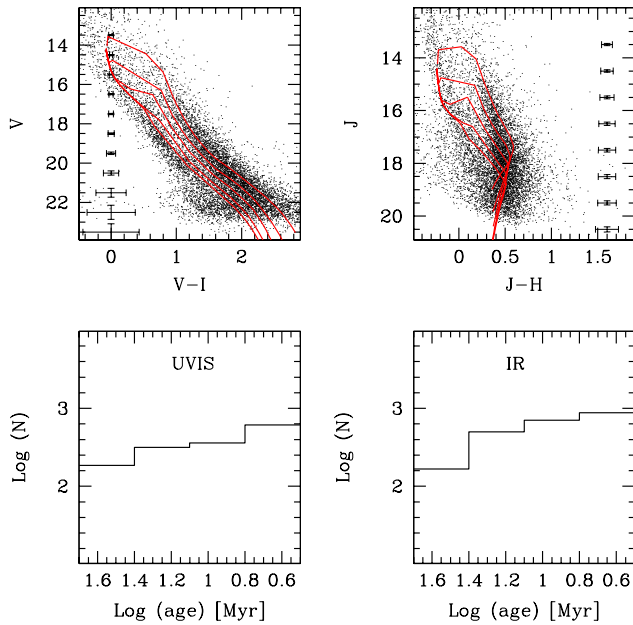


Fig. 6 Top panels: Dereddened $V, V - I$ (left panel) and $J, J - H$ (right panel) CMD of the WFC3 FoV. The population of PMS stars is fitted with 2, 5, 10, 20, 30 Myr PMS isochrones (from right to left) from DC09 (red solid lines). Photometric colour and magnitude uncertainty are reported for both CMDs. Bottom panels: logarithmic histograms representing the number of PMS stars in the cluster, in each age interval, as function of age, in UV and IR FoV. The histograms are derived from the isochrones showed in top panels.

4.4 Structure of the cluster

With these data in hand, one can begin to determine more precisely the physical structure of the cluster. To do this, we first plot the number of stars in each age bin shown in Fig. 5 inside annular rings $0.4'$ wide progressing in steps of $0.4'$ from the cluster center out to a distance of $4.8'$ well outside the nominal cluster radius. In Fig. 7 we show this radial distribution for the stars in each age bin. With these data we can confirm that the cluster itself is totally contained within the reference radius of $2.5'$ obtained by NPG02 since star number counts decrease until this value and remain constant at larger radii. Stars in all the age ranges studied show the same behaviour, indicating that all the PMS stars in our sample (old and young) definitely belong to the cluster NGC 3603 as defined in Sect. 1. Thus, all recent star formation is confined to the compact cluster.

These results also show that the objects located near the ZAMS in the CMD of Fig. 4 are not field stars, but most of them belong to the cluster population. In fact, if we assume that all the stars in the older bins, i.e. near the ZAMS, belong to the field and not to the cluster and considering a uniform contamination in the region, we would expect to obtain a flat profile, in contrast with what we observe. As expected, young stars (age 2 – 10 Myr) in the considered mass range are the most numerous ones, and they are concentrated towards the central region of the cluster (see also Sect. 4.5). This result is similar to that found in the massive cluster 30 Doradus, in the LMC (De Marchi et al. 2011a) and NGC 346 (De Marchi et al. 2011a; De Marchi, Panagia & Sabbi 2011b, in the Small Magellanic Cloud (SMC)). On the other hand, the cumulative radial distributions of young stars, defined as all the PMS stars in our sample with ages between 2 and 10 Myr (< 10 Myr) and old stars, all PMS stars with ages between 10 and 30 Myr (> 10 Myr) plotted in Fig. 8 yield an unexpected result. Although both curves are steeper within $\sim 2.5'$ and tend to flatten beyond this radius, the old/young ratio plotted in Fig. 9 obtained from these two distributions is almost flat, i.e. old stars are radially distributed roughly in the same way as the young ones. This is further evidence supporting our previous result that these stars are members of the cluster but it also shows that star formation in NGC 3603 seems to have proceeded on average uniformly across the cluster (but see the next Section for more details on this issue).

However, Fig. 7 does not give us any information about the azimuthal distribution because the number of objects is integrated over the whole area of the rings. Therefore, to better characterize the structure of the cluster, we divided each ring in two sectors of 180 degrees each, facing eastward and westward (with respect

to the Right Ascension of the cluster centre) and successively also northward and southward (with respect to the Declination of the cluster centre). We tried also to divide each ring in four sectors, but we concluded that the number of objects would drop too much providing results with poor statistics so we decided to keep the separation in the two halves described above. The results of these star count profiles are shown in Fig. 10, where it is evident that the distribution of stars in the cluster is not spherically symmetric. Actually, stars younger than 20 Myr seem more extended in the South-East (SE) direction than in the North-West (NW) one.

4.5 Spatial distribution

To better study and characterize the spatial distribution of the cluster and to get a direct visual impression of the bi-dimensional shape and distribution of the stars of different ages, we derived density maps obtained using the same age intervals as in the previous sections (see for example Fig. 7). This allows us, in particular, to look for any possible differences in spatial distribution between young and old stars. To generate the density maps, we divided the whole FoV in a grid, with a step of $0.1'$, and we counted stars inside each bin. In this way, we derived a local number density for each point across our FoV. As a first step, we calculated a mean density for the “background” analyzing only the external fields; in this way we obtained a mean density, ρ , and a standard deviation, σ that we used to derive the final maps shown in Fig. 11. In the density maps, we plotted with different colours the regions where the density is $> 3\sigma$, $> 4\sigma$, $> 5\sigma$, $> 7\sigma$ and $> 10\sigma$ over the background for each age interval, independently of the number of stars observed. We also show a contour without colour, representing the region for which the density is $> 2\sigma$, to show that stars are really concentrated in the central region and do not extend outside the nominal radius of $2.5'$.

In Fig. 11, where we zoomed the central region of the cluster, two aspects are easily observed: as already stated before, stars preferentially extend in the SE direction, rather than in the north or west ones. Moreover, it seems that the density peaks of young and old stars are located in different positions in the field. Indeed, if we observe the top left panel of Fig. 11, we see that the centre of the cluster coincides also with the density peak of stars with age between 2 and 5 Myr. On the other hand, moving towards older ages, we see in the top right panel of Fig. 11 that the region of highest density seems to be more extended with a curious shape with two lobes that encompass the centre of the cluster. Stars between 10 and 20 Myr in the bottom

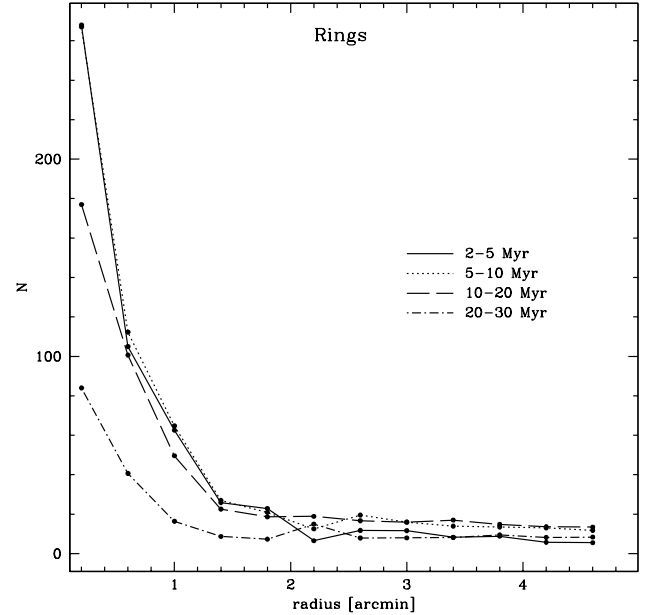


Fig. 7 Number of sources, per unit area, as a function of distance from the centre of the cluster. Solid line: stars with age between 2 and 5 Myr; dotted line: stars with age between 5 and 10 Myr; long dashed line: stars with age between 10 and 20 Myr; dotted-dashed line: stars with age between 20 and 30 Myr. All objects are mostly concentrated within $r = 2.5'$.

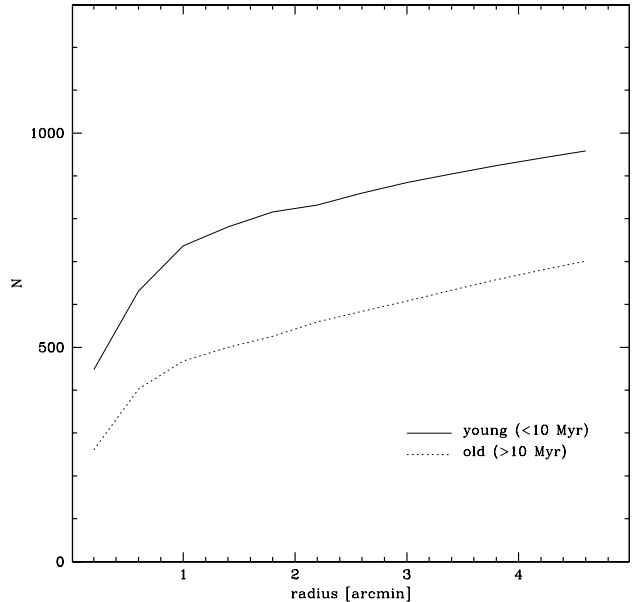


Fig. 8 Cumulative radial profiles obtained from young stars in the age interval between 2 and 10 Myr (solid line) and from old stars in the age interval between 10 and 30 Myr (dotted line). The number of young stars is substantially twice respect to the old ones. Both distributions have the same shape, with a steep increase until $r \sim 2.5'$ and a flattening beyond it.

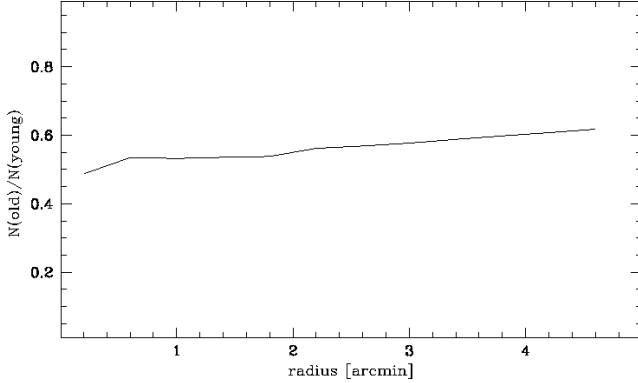


Fig. 9 Old/young ratio derived from the cumulative distributions shown in Fig. 8.

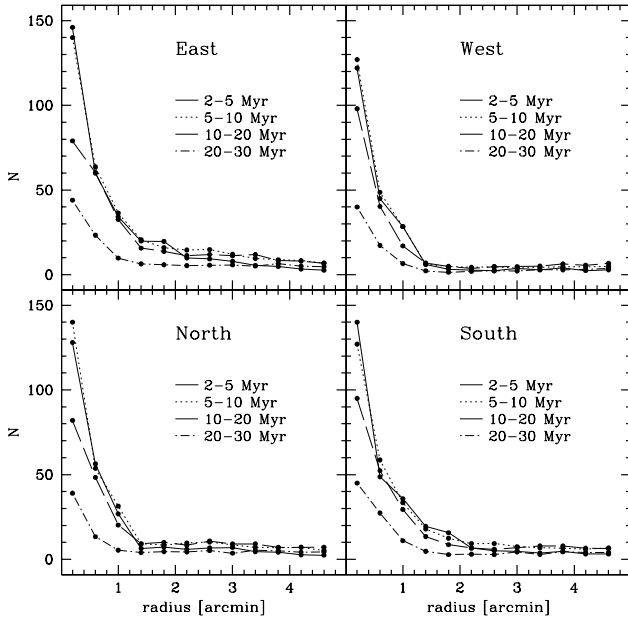


Fig. 10 Number of sources, per unit area, as a function of distance from the centre of the cluster, in the various sectors of rings. North, South must be intended respect to the Declination of the cluster centre, while East and West respect to the Right Ascension of the centre. Symbols for the lines are the same as in Fig. 7.

left panel of Fig. 11 show two peaks in the central region with the one located in the SE more pronounced. Finally, in the bottom right panel of Fig. 11 we find again a single peak of density not spatially coincident with the centre of the cluster, but rather located towards the SE.

In conclusion, all the stars in the cluster are distributed in a flattened oblate spheroidal pattern with the major axis oriented in an approximate SE-NW direction and with a flattening or length of the equatorial radius decreasing with increasing age. The density peak also shifts towards the SE with increasing age. The origin of this peculiar asymmetry is unclear but could be related to the possible tidal effects on the cluster stars by the massive gas clumps located above and below the cluster (Nürnberg et al. 2002). It may also be a reflection of the effects of sequential triggering or positive feedback of the first older generation on the younger one due to winds and shocks compressing the molecular clouds surrounding the core. The substantial tail of young stars extending to the SE of the density peak towards the prominent pillar in that direction may be tracing the region where the latter effect is most pronounced.

Curiously, the most massive stars in the core of the cluster also seem to lie along a line oriented in the same direction.

5 Systematic uncertainties of the age determination

Taken at face value, the results described so far clearly point to the cluster stars in this mass range having a continuous age spread of at least $\sim 20 - 30$ Myr, with the star formation rate increasing continuously up to at least within ~ 2 Myr of the present time. However, this result could be seriously affected by the uncertainties listed in Sect. 1. In this section, these uncertainties are considered in detail and their effect measured as accurately as possible to determine if they could alter the results described above.

5.1 Differential reddening

In our analysis so far, the possibly tried and true method of applying to all the stars an average correction for reddening in an appropriately chosen wide area was used, but this approach may lead to substantial errors if reddening changes significantly on much smaller spatial scales. In order to take this possible patchy or differential reddening into account, Pang, Pasquali & Grebel (2011, hereafter P11) used the WFC3 $H\alpha$, Paschen β filters and broad/medium

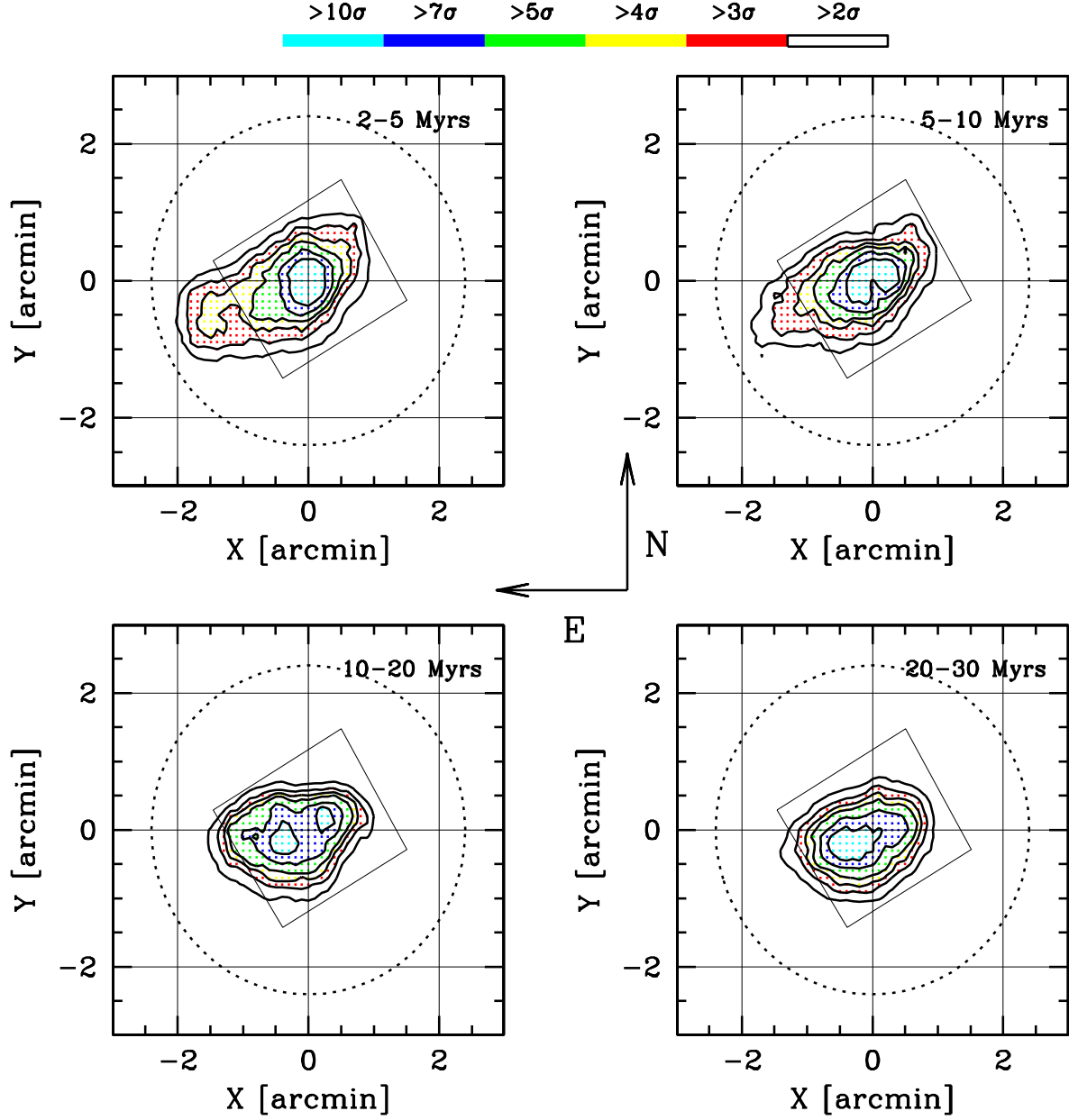


Fig. 11 Spatial distribution of stars in the same age intervals used for the radial profiles (top left panel: 2-5 Myr; top right panel: 5-10 Myr; bottom left panel: 10-20 Myr; bottom right panel: 20-30 Myr). Figure shows a zoomed region of our FoV, with an area of $3' \times 3'$, centred on the centre of the cluster determined by SB04. Colour code representing the number density of stars above the background, expressed in terms of σ , is shown in the top part of the figure, the cyan colour indicating the density peak (i.e.: $> 10\sigma$ over the background); a circular area of radius $2.5'$, representing the nominal radius of the cluster is plotted together with a square region representing the WFC3 IR FoV. Orientation of the image is also reported.

bands for the line continuum to compute the *Balmer* decrement of the gas per pixel. By applying the Fitzpatrick (1999) reddening law ($R_V = 3.1$), they derived a two-dimensional map of colour-excess, $E(B-V)$ per pixel, across the WFC3 FoV. Because the brighter stars in the core of NGC 3603 ($r < 0.52$ pc) are saturated, P11 could not measure the colour excess associated with the core. They adopted a fixed $E(B-V) = 1.51$ mag, which is the median value of the colour excess within an annulus ($0.52 < r < 1$ pc) centred on the core. This is justified by the fact that, according to SB04 (see their Fig. 5), the colour excess within 1 pc from the core changes by only 0.05 mag.

As discussed in P11, there are two sources of uncertainty in this process: the first comes from the photon noise of the images, and it varies on average from $\sigma_{E(B-V)} = 0.4$ at $E(B-V) = 1.2$ mag to $\sigma_{E(B-V)} = 0.1$ mag at $E(B-V) = 2.4$ mag. The second source of uncertainty is systematic and is due to the contribution of emission lines to the flux in the broad/medium filters used to subtract the continuum underlying the $H\alpha$ and Paschen β lines. An estimated line contamination of about 10% in all broad/medium filters increases the colour excess by 0.05 mag on average. The adopted extinction law also contributes to the systematic uncertainties. By replacing the Fitzpatrick (1999) extinction law with that of Cardelli, Clayton & Mathis (1989), the colour excess becomes smaller by 0.1 mag. On average, the systematic uncertainty is of the same order or smaller than the uncertainty due to photon noise.

Here, we assume that the dust distribution in NGC 3603 affects the gas and the stars in a similar way. Therefore, we adopt the reddening map of P11 and read from it the $E(B-V)$ at the spatial position of each star detected in the $F110W$ and $F160W$ images. We assume the Cardelli, Clayton & Mathis (1989) extinction law with $R_V = 3.55$ (from SB04) and correct for extinction the J and H magnitudes of the detected stars. An uncertainty of 0.1 mag on the $E(B-V)$ derived by P11 translates into $\Delta(J-H) = 0.05$ mag. The result of this correction for the average plus the differential reddening for the central WFC3 field is shown in the right panel of Fig. 12. For comparison, on the left panel of Fig. 12, we show the usual CMD obtained with the correction adopted so far (*i.e.*: correction with the mean value $A_V = 5.5$ for all the stars in the WFC3 FoV).

As is evident from the comparison between the two CMDs dereddened in different ways, the correction for differential reddening (right panel of Fig. 12) does not have a dramatic impact on the overall distribution of stars in the $J, J-H$ plane indicating a) that the local dust distribution is relatively uniform, b) that most of

the cluster stars lie behind the absorbing dust and c) that applying an average total extinction to the outer HAWK-I fields will not significantly affect the observed scatter of the stars there either once the appropriate local value of A_V is determined. The age histogram obtained using star by star correction in the WFC3 field is shown in Fig. 13 (dashed line), together with that using a mean value for A_V ($A_V = 5.5$, solid line).

An error in the assumption that the $E(B-V)$ of the stars is the same as that of the gas does not affect the observed stellar distribution or scatter in the CMD, as it can only translate it slightly up or down in the direction almost parallel to the isochrones, shown in Fig. 4. This uncertainty in other words would affect the mass determination, but only very marginally the age determination (see also De Marchi et al. 2011a). The same can be said also for our assumed value of R_V ; the use of other extinction ratios present in literature could only shift the whole CMD, but this collective effect cannot erase the observed age spread.

5.2 Stars with possible IR excess

Another source of uncertainty could be an error in the correct location of stars in the IR CMD due to reprocessing of photospheric emission by dust in a circumstellar cloud or disc surrounding the object. This effect gives rise to an excess that would need to be corrected for. A good handle on this effect can be obtained by looking for indications of accretion activity in the PMS stars of NGC 3603 by means of measurements of the $H\alpha$ and Paschen β line emission (contained in WFC3 F656N and F128N filters, respectively) in accreting objects (see for example Natta, Testi & Randich 2006). Among the 412 objects with $H\alpha$ emission found in B10, 255 have an IR counterpart. Exploiting the F127M and F128N filters, and with a simple colour cut, $F127M - F128N \geq 0.35$, we found 802 objects with Paschen β excess (a detailed description of the selection criterion and of the properties of these stars is beyond the scope of this paper and will be presented in a future work). Thus, the final number of stars showing an $H\alpha$ and/or Paschen β excess, is 1057. We removed them from the catalogue and we compared the age distribution obtained with and without them. We show this comparison in the left panel of Fig. 14, where the dashed line is the histogram between 2 and 30 Myr obtained without them and the solid line is that showed in Fig. 13, with all the objects and a mean A_V .

Another possibility we explored is to quantify numerically in terms of magnitude the value of this excess and to shift objects in the CMD by the appropriate amount. Cieza et al. (2005), studying a sample of classical T Tauri stars, argued that they possess significant

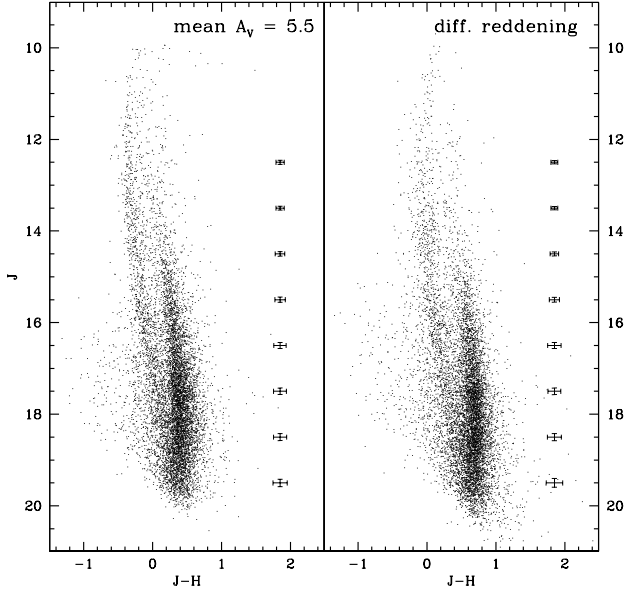


Fig. 12 Dereddened CMDs for the WFC3 field, obtained using the average total extinction, $A_V = 5.5$ (left panel), and the correction for differential reddening by P11 (right panel).

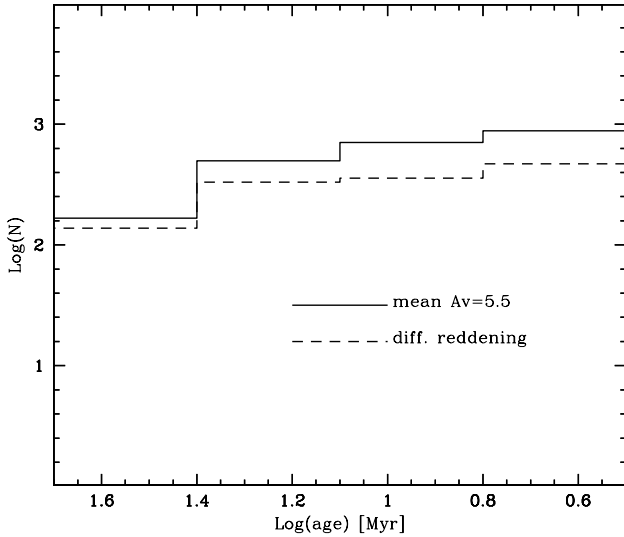


Fig. 13 Age histogram obtained using the mean $A_V = 5.5$ (solid line) compared with the histogram obtained by star-to-star correction for differential reddening from P11 (dashed line).

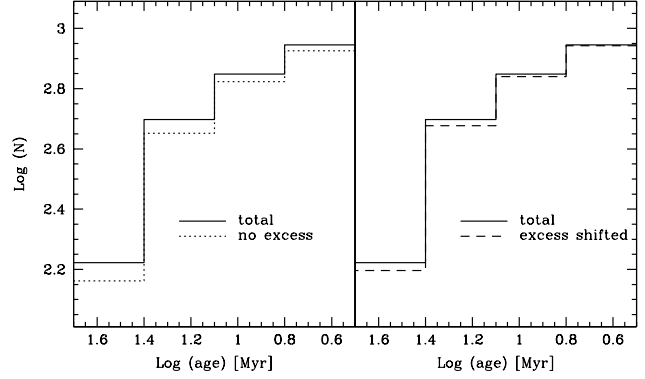


Fig. 14 Left panel: age histogram obtained removing all the sources with a possible excess (dotted line) compared with the histogram with all the objects. Right panel: age histogram obtained shifting the sources with an IR excess of a mean quantity in J and H , ($\delta < J > = 0.35$ and $\delta < H > = 0.69$, respectively) derived by Cieza et al. (2005, dashed line). As in the left panel, we show for comparison the usual histogram.

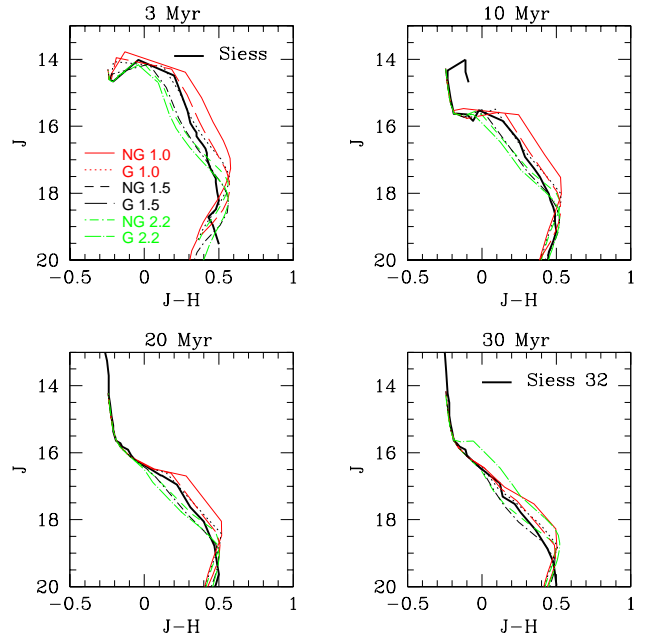


Fig. 15 The range of theoretical grey (G) and non grey atmosphere (NG) isochrones from DC09, with convection efficiency represented by α spanning from 1.0 to 2.2 plotted for 3, 10, 20, 30 Myr, together with 3, 10, 20, 32 Myr isochrones from Siess, Dufour & Fiorentini (2000) for comparison.

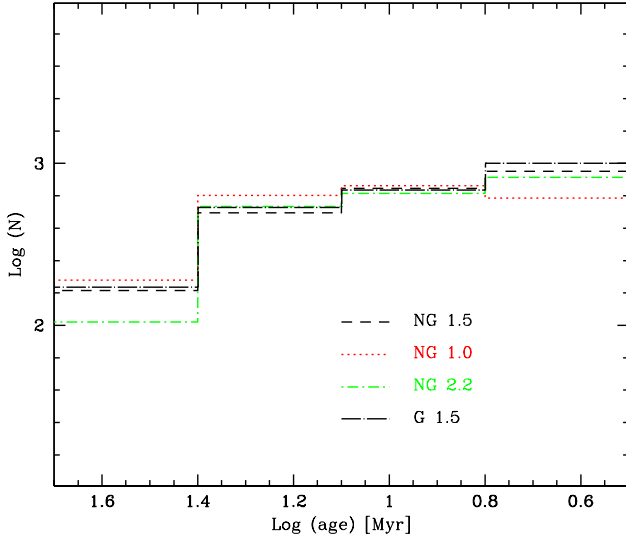


Fig. 16 Age histograms obtained using different theoretical models. The symbols for the lines are the same as in Fig. 15, so the black dashed line represents the non grey atmosphere with $\alpha = 1.5$, that is the model we adopted in this paper. Red dotted line: non grey atmosphere with $\alpha = 1.0$; green dotted-short dashed line: non grey atmosphere with $\alpha = 2.2$; black dotted-long dashed line: grey atmosphere with $\alpha = 1.5$. All models are consistent with each other, except in the last bin, due to the slight differences among isochrones (see Fig. 15)

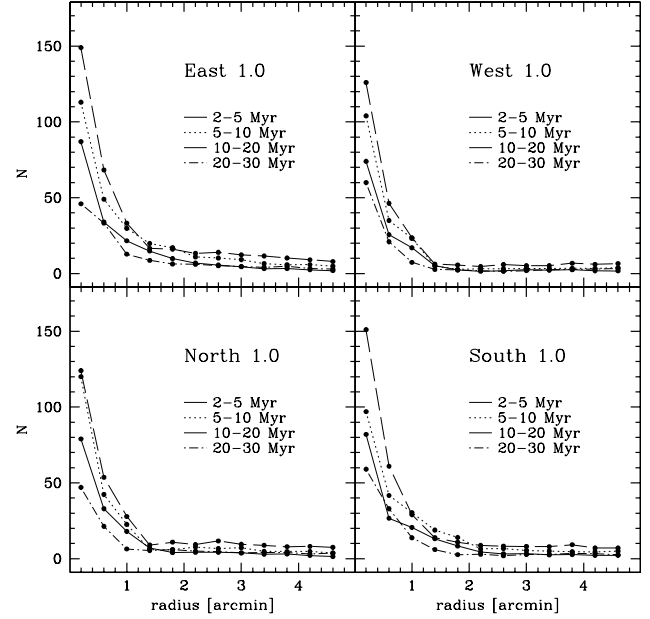


Fig. 17 Number of sources, per unit area, as a function of distance from the centre of the cluster, in the various sectors of rings, using a theoretical model with non grey atmosphere and $\alpha = 1.0$. North, South must be intended respect to the Declination of the cluster centre, while East and West respect to the Right Ascension of the centre. Symbols for the lines are the same as in Fig. 7.

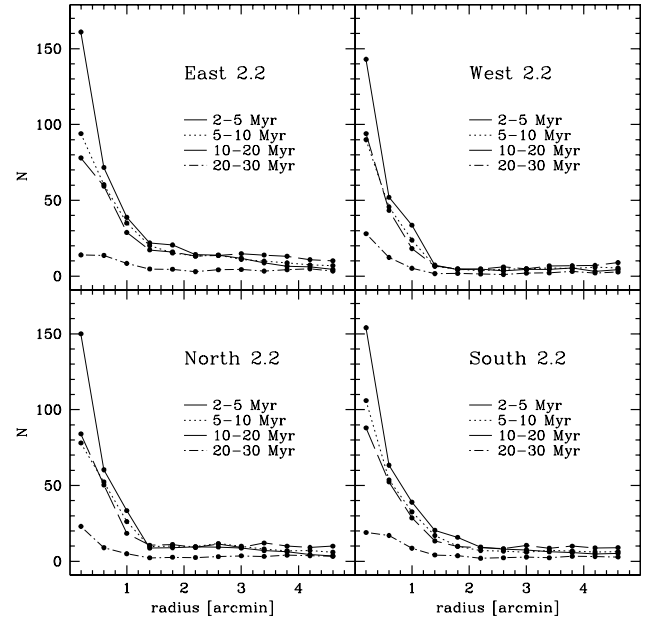


Fig. 18 Number of sources, per unit area, as a function of distance from the centre of the cluster, in the various sectors of rings, using a theoretical model with non grey atmosphere and $\alpha = 2.2$. North, South must be intended respect to the Declination of the cluster centre, while East and West respect to the Right Ascension of the centre. Symbols for the lines are the same as in Fig. 7.

non-photospheric excess in the J and H bands, and derived that the mean excess in J and H is $\delta < J > \sim 0.35$ and $\delta < H > \sim 0.69$, respectively. The age distribution obtained after applying these magnitude shifts to the 802 stars with Paschen β excess is shown in the right panel of Fig. 14. This is compared as in the left panel with the histogram with all the objects. Looking at both cases, it is evident that the trend observed is the same, either that we remove the stars or that we shift them. Moreover, the comparison with the histogram with all the objects does not show significant discrepancies. Hence, the three histograms are fully consistent within the Poisson uncertainties. We can conclude that the source of uncertainty due to IR excess in accreting stars is not a relevant problem in our work, and cannot appreciably change the results reported here.

5.3 Differences in theoretical models

In this paper we derive the ages of the stars of NGC 3603 using standard hydrostatic stellar models. This procedure rests on the assumption that neither the residual accretion after the protostellar phase nor the uncertainty in the zero point of ages affect the results in a strong way. In any case, the theoretical description of moderately low mass objects is affected by uncertainties in the description of some physical inputs, in particular convection and treatment of boundary conditions.

Since the low mass stars in the PMS are fully convective and over-adiabatic, any change in the convective model substantially alters the location of the track in the theoretical HR plane. The use of a less efficient treatment of convection (lower α) leads to a larger temperature gradients, so that, for a given luminosity, the structure readjusts on a more expanded configuration, with a subsequent shift of the track to lower effective temperatures.

In order to see the effect of the efficiency of convection on the age spread of NGC 3603 we computed a set of models with three different values of the parameter $\alpha = 1, 1.5, 2.2^2$. The path followed by the theoretical PMS tracks on the HR diagram is also dependent on the boundary conditions used to fit the numerical integration of the structural equations of the interior with the atmosphere. In fact, the use of a non grey atmospheric treatment shifts the tracks to cooler T_{eff} within an extended interval of masses and ages (Montalbán et al. 2004). In order to show the effect of grey models on

the age of the stars, for each choice of α we have also calculated models with a grey approximation.

In Fig. 15 we compare the shape of isochrones of different ages, in various models from DC09, which differ in the type of atmosphere, grey or not grey, and in the value of the parameter of the convection efficiency α . Moreover, we add to the comparison the model from Siess, Dufour & Fiorentini (2000, adopted by B10 and S11).

The effect on the age histograms of the extreme cases is shown in Fig. 16, while in Fig. 17 and Fig. 18 we show what happens to our radial profile distributions using the non grey atmosphere and adopting $\alpha = 1.0$ and $\alpha = 2.2$.

All these models assume that protostars reach their birthline by constant or slowly varying accretion. Recently, however, doubts have been expressed as to the validity of this assumption when it was realized that if, instead, protostars gain mass mainly by repeated but short lived episodes of disc accretion, it may be possible for them to end up with much smaller radii and, therefore, fainter than expected in the previous steady state accretion models. This would have the effect of making them look much older than they really are and biasing the cluster isochronal age distribution. Unfortunately, it is not yet clear at all what this means in practice since the first analyses yield contradicting results (Baraffe, Chabrier & Gallardo 2009; Hosokawa, Offner & Krumholz 2011).

Moreover, Hartmann, Zhu & Calvet (2011) have argued persuasively that the cold episodic accretion models used so far are unrealistic, in which case this scenario would end up yielding uncertainties of only ± 1 Myr in the age of low mass PMS stars well within the measured age uncertainties of the older stars in our sample. But until these issues are clarified by more theoretical and observational work, movement of some young stars across the CMD due to episodic accretion cannot be ruled out and even seems plausible, but it is quite unlikely that it would affect such a large number of older stars in our sample.

5.4 Variability and distance uncertainties

Individual stars may vary in colour and luminosity somewhat of course, but there is no indication from a comparison of our recent observations with the large number of past ones that there have been any significant changes in the shape or position of the PMS sequence in NGC 3603 that would alter in any way the conclusion discussed here. The effect of uncertainties in the distance to NGC 3603 at a level of ± 0.3 mag in the distance modulus (HEM08) translates into a vertical displacement of $J = \pm 0.3$ mag in the IR CMD shown in

²According to D'Antona & Montalbán (2003), the first value leads to a better agreement with the lithium vs. T_{eff} relation observed in young open clusters stars, while the last one allows a fit of the solar radius for non-rotating models

Fig. 4. Although this small shift could in principle have an effect as large as a factor of two on the absolute ages derived through comparison with the isochrones, this would apply in a systematic way to all objects in the field and therefore would not eliminate the age spread revealed by the CMD. This can be easily observed in Fig. 19 where we showed the usual histogram, obtained with a distance modulus of 13.90 mag, compared with the two extremes in the distance estimates (13.90 ± 0.3 mag, dashed lines). Finally, depth effects are also negligible as the cluster diameter of 10 parsec represents at most a depth variation of 10^{-3} of the cluster distance.

5.5 Unresolved binary systems

Unresolved binaries can affect the uncertainties in the cluster age spread by mimicking slightly brighter objects in the CMD and thereby being mistaken for younger objects than observed. In other words, correction for unresolved binaries would tend to flatten the age histogram shown in Fig. 5 by moving objects from the “young” to the “old” bins. A precise estimate of the magnitude of this effect is difficult in the case of NGC 3603 because its binary fraction and mass ratios have not been reliably measured so far but. Nonetheless, HEM08 have carried out a very detailed analysis of the effects that unresolved binaries would have on the observed mass function of NGC 3603 obtained with ground based imaging. In their simulations, these authors assume for NGC 3603 a binary fraction similar to that of the Orion Nebula Cluster, owing to the the similar age and massive-star population of the two clusters, and they rescale it accordingly for the different distance to NGC 3603. Following HEM08, for the mass range of interest in our work ($\sim 1 - 3 M_{\odot}$) we should assume a binary fraction of $\sim 5\%$ and a mass ratio somewhere between 0.5 and 1 (see HEM08 for details). Note that since the limiting spatial resolution on our case is that of the HAWK-I photometry, the direct comparison with the ground-based study of HEM08 is applicable. With these values, the corresponding correction to the age histograms shown in Fig. 16 for this effect would be far less than the error for each bin due to the uncertainties in the theoretical models and, therefore, of no practical consequence to the overall uncertainties in the measurement. A similar result is obtained considering the probability of optical binaries namely unresolved binaries due to projection effects that, with the resolution of the WFC3, we estimate to be less than 1% in the central WFC3 field with, therefore, negligible consequence on the measured age spread.

6 Summary and Conclusion

In this work, we set out to answer three basic questions concerning the stellar population of the NGC 3603 cluster:

1. Is the age spread discovered by B10 real or apparent?
2. Is the age spread discovered by B10 cluster wide or confined to the central quarter covered by the WFC3 observations?
3. And, if real, do the older stars actually belong to the cluster NGC 3603 or to the wider HII region surrounding it?

With the data presented here, it seems reasonable to assert that the age spread is indeed real and not due to other known sources of luminosity scatter in the CMD, and that it is cluster wide. In addition the older stars (> 10 Myr) belong to the cluster and not to the surrounding field. This means that, at least in the NGC 3603 cluster, star formation is relatively slow, progressive and, to our limited temporal resolution, continuous. It started some 20-30 Myr ago and extended almost to the present time uniformly across the entire cluster. In some areas of the cluster (IRS 9, for example) star formation is still ongoing probably because of triggering due to the impact of the winds from the hot, massive stars in the core (Melena et al. 2008). An important corollary to our present study is that we find good evidence for an asymmetric spatial distribution of the intermediate mass cluster members varying with age that is most likely due to the by now well established fact that star formation tends to occur in compact knots or cores of gas and dust located along long filaments in the natal molecular cloud. This hypothesis is made particularly plausible in our case since the large scale distribution of gas and dust in the NGC 3603 GMC is elongated in a roughly NS direction (Nürnberg et al. 2002) while on a smaller scale around the star cluster, the orientation of the molecular material tends to lie in the SE-NW direction roughly coinciding with that of the major axis of the oblate spheroid. The reason for the observed variation with age in this case would simply be due to the drift of the older stars away for their birthplace.

M.C. and F.P. acknowledge the financial support of ASI through the ASI-MICELA AE grant. We thank P. Grandi and P. Malaguti for useful discussions and suggestions and for their support of the project and M. Mutchler for precious assistance in data preparation and reduction. This paper is based on Early Release Science observations made by the WFC3 Scientific

Oversight Committee. We are indebted to the members of this committee for their support and encouragement in every facet of our work. This publication makes use of data products from the Two Micron All Sky Survey, which is a joint project of the University of Massachusetts and Infrared Processing and Analysis Center/California Institute of Technology, funded by the National Aeronautics and Space Administration and the National Science Foundation.

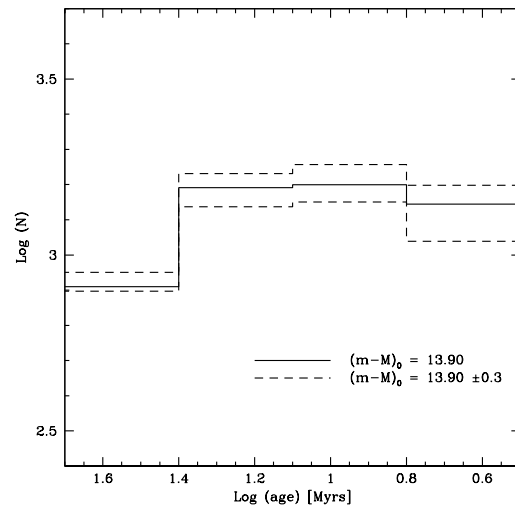


Fig. 19 Age histograms obtained using distance modulus of 13.90 mag (from HEM08), compared with the two extreme cases for the uncertainty of this value (distance modulus of 13.90 ± 0.3 mag, dashed lines).

References

- Allard, F., & Hauschildt, P.H., 1997, The NEXTGEN model grids. Web location: <http://hobbes.hs.uni-hamburg.de/yeti/midwacker.html>
- Böhm-Vitense, E. 1958, *Z. Astroph.*, 46, 1
- Allard, F., Hauschildt, P.H., & Schweitzer A., 2000, *ApJ*, 539, 366
- Baraffe, I., Chabrier, G., & Gallardo, J., 2009, *ApJL*, 702, L27
- Beccari, G., et al., 2010, *ApJ*, 720, 1108 (B10)
- Bellazzini, M., Fusi Pecci, F., Messineo, M., Monaco, L., & Rood, R. T., 2002, *AJ*, 123, 1509
- Bertin, E., & Arnouts, S., 1996, *A&AS*, 117, 393
- Cardelli, J.A., Clayton, G.C., & Mathis, J.S., 1989, *ApJ*, 345, 245
- Cieza, L.A., Kessler-Silacci, J.E., Jaffe, D.T., Harvey, P.M., & Evans II, N.J., 2005, *AJ*, 635, 422
- D’Antona, F., & Montalbán, J., 2003, *A&A*, 412, 213
- De Marchi, G., Panagia, N., & Romaniello, M., 2010, *ApJ*, 715, 1
- De Marchi, G., Panagia, N., Romaniello, M., Sabbi, E., Sirianni, M., Prada Moroni, P.G., & Degl’Innocenti, S., 2011a, *ApJ*, 740, 11
- De Marchi, G., Panagia, N., & Sabbi, E., 2011b, *ApJ*, 740, 10
- De Marchi, G., et al., 2011c, *ApJ*, 739, 27
- De Pree, C.G., Nysewander, M.C., & Goss, W.M., 1999, *AJ*, 117, 2902
- Di Criscienzo, M., Ventura, P., & D’Antona, F., 2009, *A&A*, 496, 223 (DC09)
- Dotter, A., 2007, *PhDT*, 17D
- Eisenhauer, F., Quirrenbach, A., Zinnecker, H., & Genzel, R., 1998, *ApJ*, 498, 278
- Fitzpatrick, E.L., 1999, *PASP*, 111, 63
- Grevesse, N., & Sauval, A.J., 1999, *A&A*, 347, 348G
- Harayama, Y., Eisenhauer, F., & Martins, F., 2008, *ApJ*, 675, 1319 (HEM08)
- Hartmann, L., 2003, *ApJ*, 585, 398
- Hartmann, L., Zhu, Z., & Calvet, N., 2011, *arXiv1106.3343*
- Heiter, U., et al., 2002, *A&A*, 392, 619
- Hillenbrand, L.A., 2009, in *The age of stars*, Proceedings of the International Astronomical Union, IAU Symposium, 258, 81
- Hosokawa, T., Offner, S.S.R., & Krumholz, M.R., 2011, *ApJ*, 738, 140
- Jeffries, R.D., Proceedings of JENAM10: star clusters in the era of large surveys, in press, 2011, *arXiv1102.4752J*
- Kalirai, J.S., et al., 2009, *Instrument Science Report WFC3*, 2009-30, 20 pages, 30
- Kissler-Patig, M., et al., 2008, *A&A*, 491, 941
- Mackenty, J.W., Kimble, R.A., O’Connell, R.W., & Townsend, J.A., 2010, in *Optical, Infrared and Millimeter Wave*, edited by Oschmann J.M. Jr., Clampin M.C., MacEwen, H.A., Proceedings of the SPIE, vol. 7731, 77310
- Melena, N.W., Massey, P., Morrell, N.I., & Zangari, A.M., 2008, *AJ*, 135, 878
- Melnick, J., Tapia, M., & Terlevich, R., 1989, *A&A*, 213, 89
- Montalbán, J., D’Antona, F., Kupka, F., & Heiter, U., 2004, *A&A*, 416, 1081
- Natta, A., Testi, L., & Randich, S., 2006, *A&A*, 452, 245
- Nürnberg, D.E.A., & Petr-Gotzens, M.G., 2002, *A&A*, 382, 537 (NPG02)
- Nürnberg, D.E.A., Bronfman, L., Yorke, H.W., & Zinnecker, H., 2002, *A&A*, 394, 253
- Pang, X., Pasquali, A., & Grebel, E.K., 2011, *AJ*, 142, 132 (P11)
- Preibisch, T., et al., 2011, *A&A*, 530, A34
- Rochau, B., Brandner, W., Stolte, A., Gennaro, M., Gouliermis, D., Da Rio, N., Dzyurkevich, N., & Henning, T., 2010, *ApJL*, 716, L90
- Siess, L., Dufour, E., & Forestini, M., 2000, *A&A*, 358, 593
- Skrutskie, M.F., et al., 2006, *AJ*, 131, 1163
- Spezzi, L., et al., 2011, *ApJ*, 731, 1 (S11)
- Stetson, P.B., 1987, *PASP*, 99, 191
- Stetson, P.B., 1994, *PASP*, 106, 250
- Stolte, A., Brandner, W., Brandl, B., Zinnecker, H., & Grebel, E.K., 2004, *AJ*, 128, 765
- Sung, H., & Bessell, M.S., 2004, *AJ*, 127, 1014 (SB04)
- Ventura, P., D’Antona, F., & Mazzitelli, I., 2008, *Ap&SS*, 316, 93
- Wong, M.H., et al., 2010, *Wide Field Camera 3 Instrument Handbook*, Version 2.0, Baltimore: STSCI

A Description of isochrones

The isochrones are determined by interpolating among evolutionary sequences of models of different mass, calculated by means of the ATON code for stellar evolution (Ventura, D’Antona & Mazzitelli 2008). The evolutions are followed from a fully convective configuration, with initial central temperatures T_C in the range $5.3 < \log T_C < 5.8$, until the beginning of the core H-burning phase. Both the deuterium and lithium PMS burning are followed. The chemistry used is $(X, Y, Z) = (0.70, 0.28, 0.02)$; the distribution of the heavy elements follows the solar mixture by Grevesse & Sauval (1999). The initial mass fraction of Deuterium is $X(D) = 2 \times 10^{-5}$. These models are based on up to date physics and updated non grey atmosphere models were used based on the NextGen models by Allard & Hauschildt (1997), complemented by the low gravity models by Allard, Hauschildt & Schweitzer (2000). Following a suggestion by Heiter et al. (2002), we match the atmospheric grid with the interior integration at $\tau = 10$. This choice should minimize the consistency problems related to the different EOS and opacities adopted in the interior and in the atmosphere, and to the absence of turbulence pressure in the atmospheric modeling. The temperature gradient within regions unstable to convection is found by the Mixing Length Theory, with the free parameter $\alpha = 1.5$. This choice for α accounts for the smaller efficiency of convection in the PMS phase, as indicated by the location in the HR diagram of the few objects for which the mass is known, and by the Lithium vs Mass pattern detected in young open clusters (D’Antona & Montalbà 2003). The L and T_{eff} values, are then transformed into the different observational magnitudes using the synthetic colour transformations kindly provided by (see Dotter 2007, and references therein).